Full-Wave Simulation of Electromagnetic Coupling Effects in RF and Mixed-Signal ICs Using a Time-Domain Finite-Element Method

Daniel A. White, *Member, IEEE,* and Mark Stowell

***Abstract*—This paper describes the computer simulation and modeling of distributed electromagnetic coupling effects in analog and mixed-signal integrated circuits. Distributed electromagnetic coupling effects include magnetic coupling of adjacent interconnects and/or planar spiral inductors, substrate coupling due to stray electric currents in a conductive substrate, and full-wave electromagnetic radiation. These coupling mechanisms are inclusively simulated by solving the full-wave Maxwell's equations using a three-dimensional (3-D) time-domain finite-element method. This simulation approach is quite general and can be used for circuit layouts that include isolation wells, guard rings, and 3-D metallic structures. A state-variable behavioral modeling procedure is used to construct simple linear models that mimic the distributed electromagnetic effects. These state-variable models can easily be incorporated into a VHDL-AMS simulation providing a means to include distributed electromagnetic effects into a circuit simulation.**

***Index Terms*—Behavioral modeling, finite element, substrate coupling, time domain.**

I. Introduction

DISTRIBUTED electromagnetic coupling effects are becoming increasingly important in RF and mixed analog/digital (D/A)-signal integrated circuits (ICs). This is due to a combination of higher operating frequencies and increased circuit density. It is well known that, at moderate operating frequencies, metal interconnects are not ideal and the self-capacitance and inductance of these interconnects must be taken into account. For broad-band RF circuits, the frequency dependence of the resistance, capacitance, and inductance of interconnects is important. The same can be said for other metallic structures such as planar spiral inductors, transformers, Lange couplers, etc. Determining the small parasitic capacitance and inductance of a structure, or determining the frequency-dependent S-parameters, is often referred to as parasitic extraction. Analytical models of parasitic effects in interconnects are reviewed in [1], parasitic models of integrated RF inductors and transformers are reviewed in [2], and examples of parasitic-aware RF design include [3] and [4]. In addition to analytical models, numerous numerical algorithms have been developed for static and low-frequency parasitic extraction [5]–[11].

Manuscript received October 21, 2003; revised December 25, 2003. This work was supported in part by the Defense Advanced Research Projects Agency under the NeoCAD Program.

The authors are with the Lawrence Livermore National Laboratory, Livermore, CA 94551 USA (e-mail: dwhite@llnl.gov; stowell1@llnl.gov).

Digital Object Identifier 10.1109/TMTT.2004.827008

In addition to local parasitics, long-range distributed electromagnetic effects such as substrate coupling are important. Substrate coupling is a general term to describe electromagnetic coupling of distinct components via electric currents in the common substrate. This has been demonstrated to be important in mixed-signal circuits where digital switching injects current into the substrate [12]–[16], and it has also been demonstrated that interconnects [17] and inductors [18] can also inject currents into the substrate. The substrate currents can negatively impact sensitive analog circuitry such as oscillators [19]–[21], amplifiers [22], [4], [23], and D/A converters [24]. Both passive and active guard rings have been designed to mitigate the effects of substrate coupling [25], [26], [2].

Several approaches have been proposed for modeling substrate coupling, such as lumped *RC* macromodels [27]–[30], volumetric finite-difference methods [31]–[33], and boundary-element methods [34], [35], [2]. These approaches are valid for static and low-frequency operational conditions, but do not account for wave or radiation effects, which become important when $\omega\epsilon \geq \sigma$.

In this paper, an unstructured grid finite-element method is used to simulate distributed electromagnetic coupling. The complete Maxwell's equations are solved and, therefore, parasitics, substrate currents, wave propagation, and radiation effects are included. The finite-element method employs a three-dimensional (3-D) unstructured computational mesh that is well suited for complex 3-D geometries, the media need not be planar or homogeneous and, therefore, isolation wells and guard rings can easily be simulated. The particular finite-element method used here employs the so-called "edge" or $H(\mathrm{curl})$ basis functions that are reviewed in the texts [36]–[38]. These finite elements correctly model the jump discontinuity of fields and currents across material discontinuities and they prohibit spurious solutions that appear when using standard node-based finite-element method. The Maxwell equations are solved directly in the time domain using a stable and energy conserving time-stepping algorithm [39]–[41], and the results are second-order accurate in space and time even for distorted computational meshes [42]. By computing directly in the time domain, it is possible to generate data covering from dc to 100 GHz in a single simulation.

With this full-wave simulation approach, it is possible to visualize the computed distributed fields and currents and, therefore, gain insight into the coupling process, leading to improved designs. In addition, it is possible to construct reduced-order behavioral models of the full-wave coupling and incorporate these models into a circuit simulation to determine the effect of elec-

0018-9480/04$20.00 © 2004 IEEE

tromagnetic coupling on the circuit operation. In this paper, we propose a state-variable model for the coupling [43], [44]. Once input and output ports have been identified, the state-variable model of the coupling between these ports is computed automatically. The state-variable approach was chosen because it is mature and widely used in signal processing and control applications, and also because it is amenable to mixed-signal simulation via VHDL-AMS [45], [46]. VHDL-AMS is a language for simulation of combined discrete-event and continuous systems, where the continuous system is a differential-algebraic system of ordinary differential equations [47], [48]. This VHDL-AMS approach has successfully been used for behavioral modeling of RF ICs [49], [50], although these previous efforts were focused on parasitics and not distributed electromagnetic coupling.

II. Finite-Element Discretization

The starting point for the full-wave simulation of distributed electromagnetic coupling effects is the time-dependent Maxwell's equations defined in the volume Ω as follows:

$$\frac{\partial}{\partial t}\vec{B} = -\nabla \times \vec{E} \tag{1}$$

$$\varepsilon\frac{\partial}{\partial t}\vec{E} = \nabla \times \frac{1}{\mu}\vec{B} - \sigma\vec{E} - \vec{J} \tag{2}$$

$$\nabla \cdot \varepsilon\vec{E} = 0 \tag{3}$$

$$\nabla \cdot \vec{B} = 0 \tag{4}$$

where $\vec{E}$ is the electric field, $\vec{B}$ is the magnetic flux density, and $\vec{J}$ is an independent current source. The fields and currents are functions of space and time. The dielectric permittivity ε, magnetic permeability μ, and electrical conductivity σ are, in general, tensors and functions of space and time. In this paper, it is assumed that ε and σ are time independent, and μ is that of vacuum (i.e., nonmagnetic materials). Note that we have assumed zero charge density in (3), but this does not preclude bound polarization charge density on material interfaces. Equations (1) and (2) can be combined to yield a second-order vector wave equation for the electric field

$$\varepsilon\frac{\partial^2}{\partial t^2}\vec{E} = -\nabla \times \frac{1}{\mu}\nabla \times \vec{E} - \sigma\frac{\partial}{\partial t}\vec{E} - \frac{\partial}{\partial t}\vec{J} \text{ in } \Omega. \tag{5}$$

This is the primary partial differential equation that will be solved by the finite-element method. Note that if the magnetic flux density $\vec{B}$ is required, it can be computed by simply integrating (1). If the independent current source $\vec{J}$ satisfies $\nabla \cdot \vec{J} = 0$, then the divergence conditions (3) and (4) can be considered initial conditions, i.e., they are implicitly satisfied for all time if they are initially satisfied. In practice, it is assumed the initial fields $\vec{E}$ and $\vec{B}$ are zero, and the problem is excited either by the independent current source $\vec{J}$ or a time-dependent boundary condition on $\vec{E}$. The vector wave equation is not completely specified until the boundary conditions on $\vec{E}$ are specified. The boundary of the problem Γ can be decomposed into nonoverlapping boundaries Γ_1, Γ_2, and Γ_3 with boundary conditions

$$\hat{n} \times \vec{E} = \vec{f}_D \text{ on } \Gamma_1 \tag{6}$$

$$\hat{n} \times \nabla \times \vec{E} = \vec{f}_N \text{ on } \Gamma_2 \tag{7}$$

$$\hat{n} \times \nabla \times \vec{E} + \hat{n} \times \eta\frac{\partial}{\partial t}\vec{E} \times \hat{n} = \vec{f}_I \text{ on } \Gamma_3. \tag{8}$$

These boundary conditions are the Dirichlet, Neumann, and impedance boundary conditions, respectively. The Dirichlet boundary condition is used to enforce a prescribed tangential electric field (or voltage) with $f_D = 0$ corresponding to the case of a perfect electrical conductor. The Neumann boundary condition with $f_N = 0$ corresponds to a perfect magnetic conductor and is also used to enforce electric field symmetry planes. The impedance boundary condition is most often used to approximate the Silver–Muller radiation boundary condition of waves radiating into an open space with $\eta = 377$ and $f_I = 0$ corresponding to the plane-wave (or first order) approximate radiation boundary condition.

There are numerous approaches that can be applied to discretize the vector wave equation. In this paper, a method-of-lines approach is used, where a finite-element procedure is used to discretize space, and a finite-difference method is used to integrate in time. The specific finite-element procedure used here is the Galerkin method in conjunction with the $H(\text{curl})$ or "edge" basis functions originally proposed by Nédélec [51]. The key properties of these basis functions are reviewed in the literature [36], [37], [52]. The emphasis of the literature is on static and frequency-domain simulation, but the same spatial discretization can be used for time-dependent simulation. Equation (5) is multiplied by a suitable test function $\vec{\Psi}$ and the resulting equation is integrated over the entire domain Ω, and an integration-by-parts formula (Green's second vector identity) is used on the $\nabla \times \nabla \times$ term. The resulting Galerkin form of (5) is then

$$\text{find } \vec{E} \in H(\text{curl};\Omega) \text{ that satisfies } \hat{n} \times \vec{E} = \vec{f}_D \text{ on } \Gamma_1$$

and

$$\left(\varepsilon\frac{\partial^2}{\partial t^2}\vec{E}, \vec{\Psi}\right) = \left(\frac{1}{\mu}\nabla \times \vec{E}, \nabla \times \vec{\Psi}\right) - \left(\sigma\frac{\partial}{\partial t}\vec{E}, \vec{\Psi}\right) - \left(\frac{\partial}{\partial t}\vec{J}, \vec{\psi}\right) - \langle \hat{n} \times \nabla \times \vec{E}, \hat{n} \times \vec{\psi}\rangle,$$

$$\text{for all } \vec{\psi} \text{ in } H_0(\text{curl} : \Omega)$$

where $(\cdot,\cdot)$ represents an inner product on Ω and $\langle\cdot,\cdot\rangle$ represents an inner product on Γ. The space $H(\text{curl})$ is the curl-conforming space

$$H(\text{curl};\Omega) = \left\{\vec{W} \in L(\Omega)^2, \nabla \times \vec{W} \in L(\Omega)^2\right\}$$

$$H_0(\text{curl};\Omega) = \left\{\vec{W} \in H(\text{curl}), \hat{n} \times \vec{W} = 0 \text{ on } \Gamma_1\right\}.$$

The last term in the variational equation is the boundary condition term. Note that the Dirichlet boundary condition on Γ_1 is dealt with as a constraint, and we can safely ignore the Neumann boundary conditions on Γ_2 in this paper. Therefore, the last term in the variational equation then consists solely of the approximate radiation boundary and can be expressed as

$$\langle \hat{n} \times \nabla \times \vec{E}, \hat{n} \times \vec{\psi}\rangle = \langle \eta\hat{n} \times \vec{E}, \hat{n} \times \psi\rangle + \langle f_I, \vec{\psi}\rangle. \tag{9}$$

The term $\langle f_I, \vec{\psi}\rangle$ is a correction term to account for deviation from a plane wave. This correction term is important if it is desired to have the mesh boundary in close proximity to the sources or scatterers and could, in principle, be computed via a

boundary-integral method [53]. However, in this paper, the correction term is ignored, resulting in the standard Silver–Muller absorbing boundary condition (ABC). The finite-element formulation also permits the use of Maxwellian perfectly matched layers (PMLs) to absorb outgoing waves, and this approach has been used in other higher frequency applications [39]. However, due to the relatively large wavelength (compared to the dimension of the circuit), the PML was not any more effective than the simpler ABC.

The volume Ω is discretized via a standard conforming finite-element mesh consisting of either hexahedra, tetrahedra, or prisms. The mesh resolution must be fine enough to capture the geometric details of the circuit. A set of finite-element basis functions is defined on the mesh, and the set of basis functions $\{\vec{W}\}$ is a discrete version of the space $H(\mathrm{curl})$. Within each element, the electric field is expanded in terms of finite-element basis functions as

$$\vec{E}(\vec{x},t)=\sum_{i=0}^{N} e_i(t)\vec{W}_i(\vec{x}) \tag{10}$$

where $\vec{W}_i$ are the finite-element basis functions and the scalars e_i are the coefficients of the basis function expansions, often called the degrees of freedom or simply the "unknowns." For the lowest order $H(\mathrm{curl})$ basis functions, the basis functions satisfy

$$\int \vec{W}_i \cdot \hat{t}_j dl = \delta_{ij} \tag{11}$$

where $\hat{t}_j$ is the unit tangent to the mesh edge j. Hence, the degrees of freedom are the voltages along the mesh edges, and there is one basis function $\vec{W}_i$ for every edge in the mesh. The test functions $\vec{\psi}$ are also chosen to be from $\{\vec{W}\}$, which is the key step in the Galerkin method. This results in a semidiscrete coupled system of ordinary differential equations

$$\mathbf{M}\frac{\partial^2}{\partial t^2}\mathbf{e}=-\mathbf{S}\mathbf{e}-\mathbf{G}\frac{\partial}{\partial t}\mathbf{e}-\mathbf{M}\frac{\partial}{\partial t}\mathbf{j}-\mathbf{R}\frac{\partial}{\partial t}\mathbf{e} \tag{12}$$

where $\mathbf{e}$ is a vector of electric field degrees of freedom and $\mathbf{j}$ is the discrete current source. The matrices in (12) are given by

$$\begin{aligned}\mathbf{M}_{ij}&=\left(\varepsilon\vec{W}_i,\vec{W}_j\right)\\ \mathbf{S}_{ij}&=\left(\frac{1}{\mu}\nabla\times\vec{W}_i,\nabla\times\vec{W}_j\right)\\ \mathbf{G}_{ij}&=\left(\sigma\vec{W}_i,\vec{W}_j\right)\\ \mathbf{R}_{ij}&=\left\langle\eta\hat{n}\times\vec{W}_i,\hat{n}\times\vec{W}_j\right\rangle.\end{aligned}$$

The well-known Newmark-beta time integration method [54], which is based on second-order central difference approximations to $(\partial^2/\partial t^2)$ and $(\partial/\partial t)$, is used to complete the discretization. The resulting update equation is

$$\begin{aligned}&\left(\mathbf{M}+\beta\Delta t^2\mathbf{S}+\Delta t/2(\mathbf{G}+\mathbf{R})\right)\mathbf{e}^{k+1}\\ &\quad=\left(2\mathbf{M}-\Delta t^2(1-2\beta)\mathbf{S}\right)\mathbf{e}^{k}\\ &\qquad-\left(\mathbf{M}+\beta\Delta t^2\mathbf{S}-\Delta t/2(\mathbf{G}+\mathbf{R})\right)\mathbf{e}^{k-1}-\Delta t^2\mathbf{M}\mathbf{j}'\end{aligned} \tag{13}$$

where $\mathbf{e}^k$ is the vector of electric field degrees of freedom at the kth time step. Note that we assume the time derivative of the current source J, denoted by $\mathbf{j}'$, can be provided. This method involves a parameter β that is used to control the stability of the method. When $\beta=0$, the method corresponds to the standard leapfrog method, which is conditionally stable, and when $0.25<\beta<0.5$, the method is unconditionally stable and nondissipative (other than physical dissipation due to conductive and radiative losses) [55], [41]. This method assumes that the time step Δt remains constant throughout the simulation.

This method requires that a large sparse linear system be solved at every time step. The final step is enforcement of the Dirichlet boundary conditions, which is done as part of the linear solution process. A subset of the electric field degrees of freedom $\mathbf{e}^{k+1}$ are simply constrained to have prescribed values determined by (6). Since the system is symmetric positive definite, the conjugate gradient method can be employed, and preconditioners may be used to accelerate convergence if large time steps are used. For the simulations performed in Section III, a diagonally scaled conjugate gradient method was used, and the system was solved to within a relative tolerance of 10^{-9} and required approximately 100 iterations per time step on average.

The time-domain finite-element method described here is second-order accurate in both space and time, is provably stable, and conserves charge and energy. The method also allows for jump discontinuity of fields and currents across material interfaces. Note that this time-domain finite-element method reduces to the well-known finite-difference time-domain (FDTD) method for the specific case of a Cartesian mesh, a β of zero, and the trapezoidal rule for effecting the volume and surface integrals [40]. The primary benefit of the finite-element method is that essentially arbitrary geometry can be modeled by an unstructured mesh, thus, there is no difficulty in simulating multiple dielectric and/or conductive layers, isolation wells and guard rings, or vertical interconnects. For simple problems consisting of a few metallic structures, boundary-element methods, which require a surface mesh for every material interface rather than a volumetric mesh, can be more computationally efficient. Fast time-domain boundary-element methods for IC applications are at present an important and interesting area of research. Nevertheless, it is demonstrated in Section III that the time-domain finite-element method is a general and powerful method that can be used to simulate full-wave distributed electromagnetic effects in ICs.

III. Example: VCO Test Circuit

A. Time-Domain Finite-Element Method Simulation Results

As an example, the time-domain finite-element method described above is applied to a voltage controlled oscillator (VCO) test circuit. The VCO was designed by Allstot's Mixed Signal Group at the University of Washington, Seattle. The schematic is shown in Fig. 1, and the layout is shown in Fig. 2. This is a test circuit designed to allow for measuring the effect of distributed electromagnetic coupling effects. There are several surrounding inductors, which are not directly connected to the VCO circuit; however, a test signal can be applied to these surrounding inductors to determine the effect on the VCO. Thus, this test circuit mimics a system-on-chip (SoC). The circuit was designed for

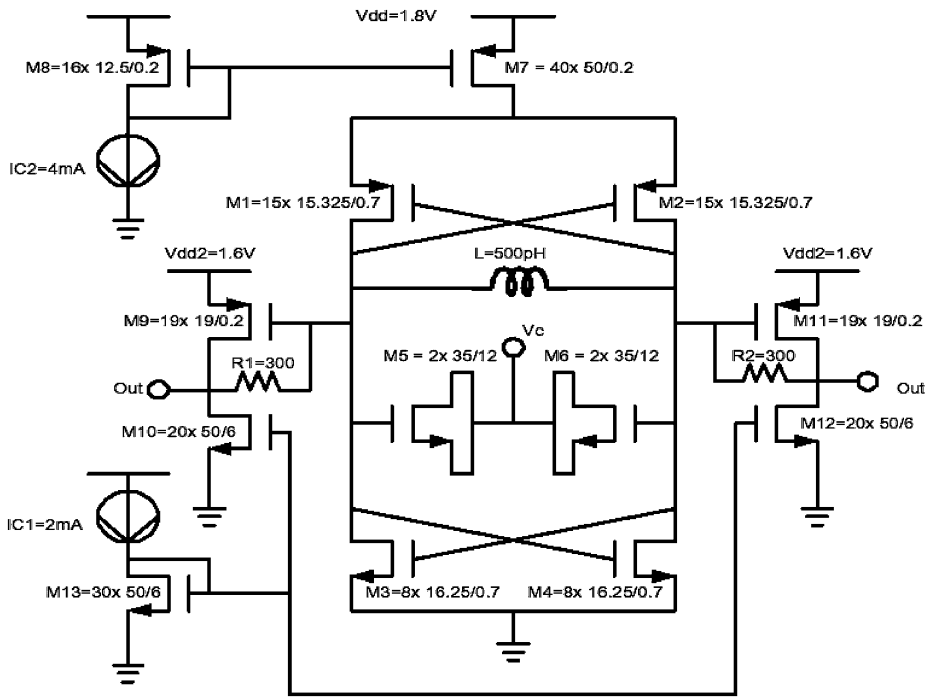

Fig. 1. Schematic of the 5.6-GHz VCO.

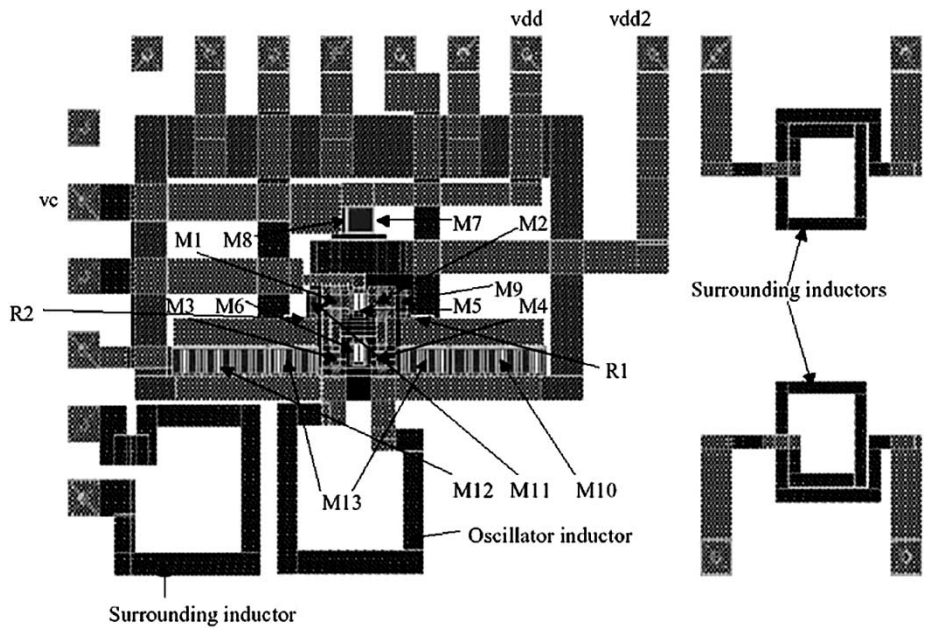

Fig. 2. Layout of the 5.6-GHz VCO.

the Massachusetts Institute of Technology Lincoln Laboratory (MITLL) 0.18-μm fully depleted silicon-on-insulator (FDSOI) CMOS process.

The test wafer contained multiple individual ICs. An area of dimension 5488 μm $\times$ 4378 μm was chosen; this area contained the VCO of interest, as well as additional circuitry and surrounding test inductors. The commercial mesh generator MicroMesh from the CFD Research Corporation (CFDRC), Huntsville, AL, was used to generate the computational mesh. The input to MicroMesh was a GDSII file of the actual layout. The metal interconnects were 20–75 μm wide and 2-μm thick. A top view of the chosen area is shown in Fig. 3, a 3-D view (with exaggerated z thickness) is shown in Fig. 4. The computational mesh consisted of 361 305 nodes and 343 200 hexahedral elements.

For the electromagnetic simulation, the surrounding inductors were terminated with a 50-Ω resistance, and the ports such as V_{dd} and V_c were left open. The voltage across the $L = 500$ pH oscillator inductor was chosen to be the "response" port, which is labeled "Z" in Fig. 3. A time-varying voltage is applied to one of the surrounding inductors labeled "A"–"F" in Fig. 3, the electromagnetic fields and currents are solved throughout the entire

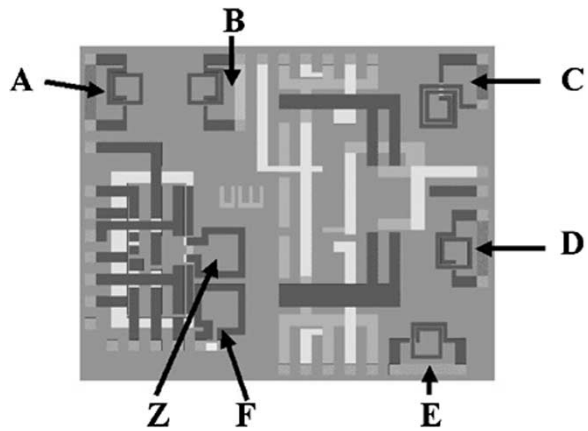

Fig. 3. Layout of the simulation area. In this figure, the VCO is in the lower left corner. The labels "A"–"F" indicate the surrounding inductors that are not part of the VCO circuit, but are fabricated for testing purposes. The inductor labeled "Z" is part of the VCO.

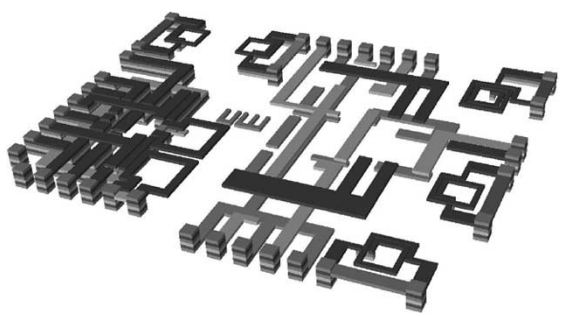

Fig. 4. 3-D view of the inductors and interconnects.

volume, and the induced voltage and current across the oscillator inductor "Z" is recorded as a function of time. Note that the response can be recorded at an arbitrary number of ports, but each excitation port requires a new simulation. The voltage excitation was chosen to be a delayed Gaussian of the form

$$v(t) = e^{-a(t-t_0)^2} \tag{14}$$

with $t_0 = 5.0 \cdot 10^{-11}$ s and $a = 2.0 \cdot 10^{21}$. This pulse contains significant frequency content in the 0–50-GHz range. The time step for the simulation was chosen to be $\Delta t = 10^{-13} s$ and the simulation was run for 6000 time steps for a total of $6.0 \cdot 10^{-10}$ s. This is a very short time from the circuit point-of-view, however, it was enough time for an electromagnetic wave to traverse the chosen area several times and to visualize the resonances of the inductors and interconnects. The simulations required several gigabytes of memory and approximately 30 h of CPU time on a high-end workstation. The majority of the computer memory was used to store the finite-element matrices, and the majority of the CPU time was spent in the linear solver.

As illustrations of how the resulting data can be visualized, Figs. 5–7 show the computed time-maximum electric-field intensity when the excitation is applied to inductors "A," "B," and "F," respectively. The simulation is 3-D, the figures are of a slice through the 3-D data. Clearly the field is most intense in the vicinity of the source, but the details of the field pattern are complex and would not have been well approximated by a simple lumped *RC* approximation of the common substrate. Figs. 8–10 show the excitation and response voltages for the

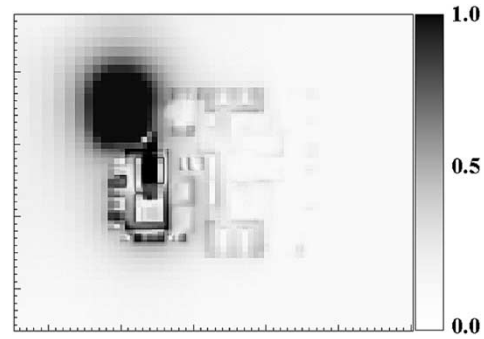

Fig. 5. Time-maximum electric-field intensity with excitation at inductor "A." This is a linear gray-scale image with black representing the maximum (1.0) and white representing the minimum (0.0).

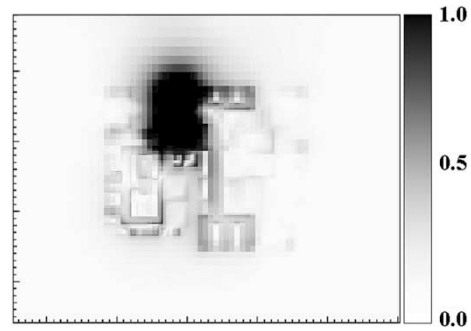

Fig. 6. Time-maximum electric-field intensity with excitation at inductor "B." This is a linear gray-scale image with black representing the maximum (1.0) and white representing the minimum (0.0).

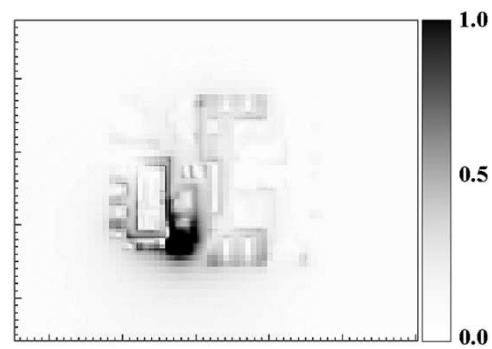

Fig. 7. Time-maximum electric-field intensity with excitation at inductor "F." This is a linear gray-scale image with black representing the maximum (1.0) and white representing the minimum (0.0).

simulations. In each figure, the response is scaled so that it is visible on the same plot. These figures clearly show the delay of the response and the resonant nature of the interconnect structure. The actual magnitude of the response voltages is given in Table I B. The magnitude of the response is correlated with distance between the excitation inductor and inductor "Z," but it is not a simple two-dimensional (2-D) $\log(r)$ or 3-D $1/r$ scaling, as would be predicted by a static calculation. The magnitude of the response depends critically upon the exact configuration of the metal interconnects in the vicinity of the inductors. These induced voltages may be strong enough to affect the operation of the VCO. In order to facilitate a circuit simulation that includes these distributed electromagnetic effects behavioral models of signals can generated.

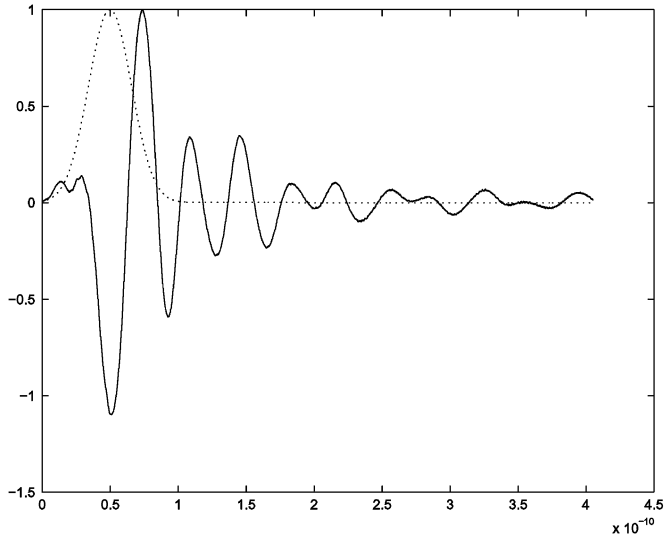

Fig. 8. Response signal at inductor "Z" (solid line) due to excitation at inductor "A" (dashed line). The response signal has been scaled by a factor of 142.

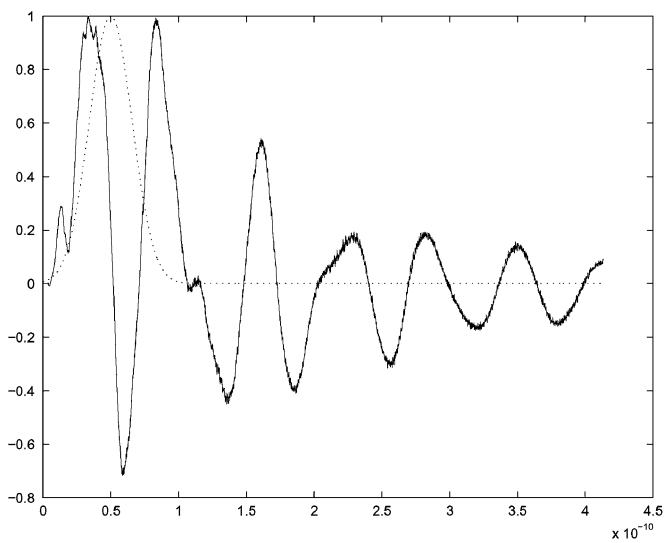

Fig. 9. Response signal at inductor "Z" (solid line) due to excitation at inductor "B" (dashed line). The response signal has been scaled by a factor of 500.

B. State-Variable Behavioral Modeling

In order to include the above-described full-wave electromagnetic results in a circuit simulation, a linear state-variable behavioral model is used. The general model equations are given by

$$dx/dt = \mathbf{A}x(t) + \mathbf{B}u(t) + \mathbf{K}e(t) \tag{15}$$

$$y(t) = \mathbf{C}x(t) + \mathbf{D}u(t) \tag{16}$$

where $x(t)$ is the state variable, $y(t)$ is the output, $u(t)$ is the excitation, and $e(t)$ is a noise signal. The order of the model is the dimension of the state vector and, in this particular application, the output and excitation are dimension 1. The matrices $\mathbf{A}$–$\mathbf{D}$, and $\mathbf{K}$ are constant coefficient matrices. The goal is to compute a low-order model that adequately represents the full-wave electromagnetic results. The problem of determining a model given the input and output data is referred to as "system identification" in the control and signal-processing communities. State-variable models for the modeling of the electromagnetic response are chosen for two reasons. First, these models are well understood and there is a wealth of algorithms and software (commercial and public domain) for generating models given the input and output

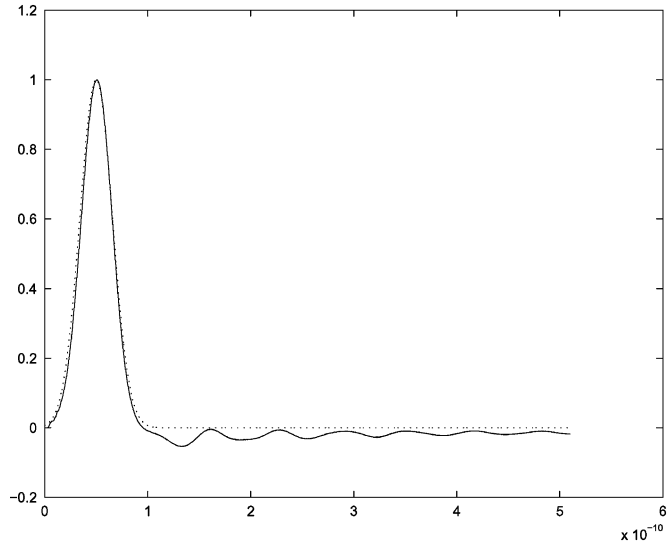

Fig. 10. Response signal at inductor "Z" (solid line) due to excitation at inductor "F" (dashed line). The response signal has been scaled by a factor of nine.

TABLE I
SUMMARY OF STATE-VARIABLE MODELS FOR MODELING THE SIMULATED ELECTROMAGNETIC RESPONSE

excitation	delay	max signal	order	fit
A	$40*10^{-13}$	$7.0*10^{-3}$	6	87
B	$30*10^{-13}$	$2.0*10^{-3}$	34	82.7
C	$50*10^{-13}$	$3.0*10^{-4}$	20	66.1
D	$65*10^{-13}$	$2.2*10^{-2}$	10	85
E	$30*10^{-13}$	$2.5*10^{-2}$	15	86.6
F	$10*10^{-13}$	$1.1*10^{-1}$	11	99.5

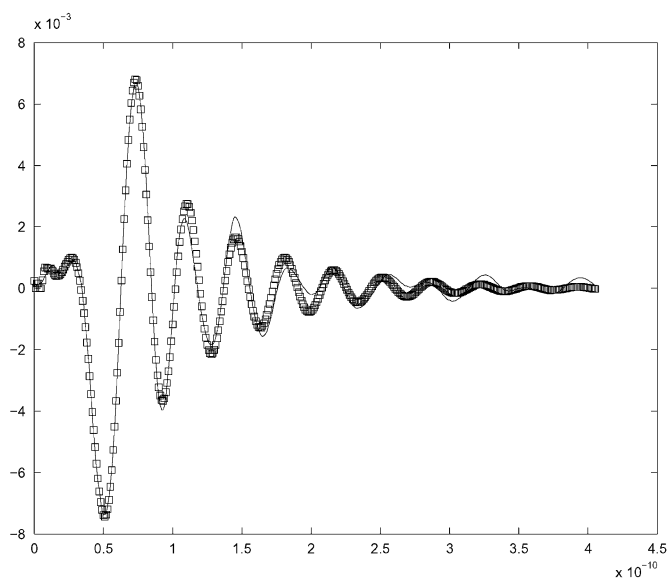

Fig. 11. Comparison of the actual electromagnetic response with the model signal for case "A." The model is designated by squares, the actual signal is the solid line. The state-variable model was of order 8 and the prediction error was within 85%.

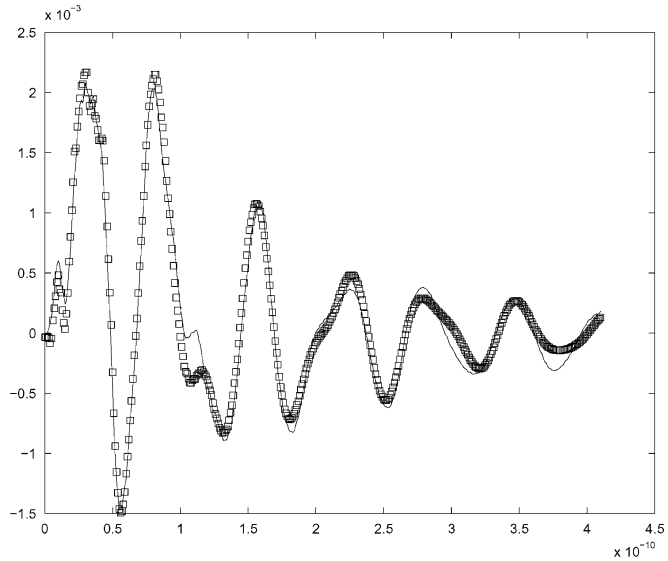

Fig. 12. Comparison of the actual electromagnetic response with the model signal for case "B. "The model is designated by squares, the actual signal is the solid line. The state-variable model was of order 34 and the prediction error was within 82%.

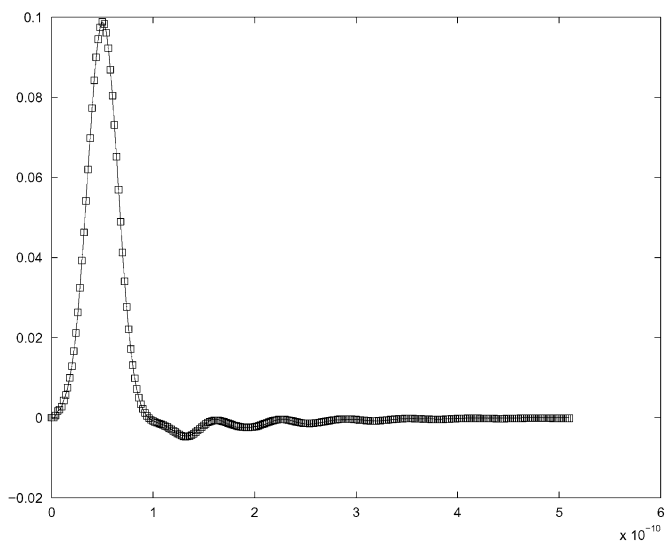

Fig. 13. Comparison of the actual electromagnetic response with the model signal for case "F." The model is designated by squares, the actual signal is the solid line. The state-variable model was of order 11 and the prediction error was within 99%.

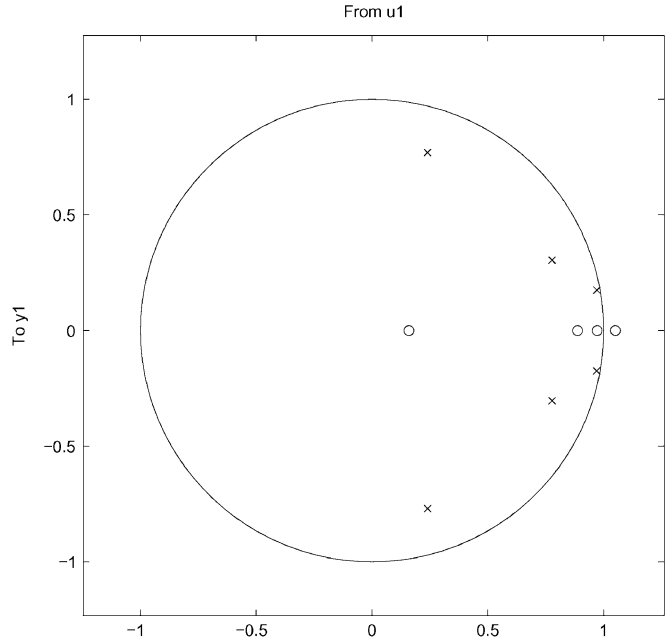

Fig. 14. Pole-zero plot for the computed linear model for case "A."

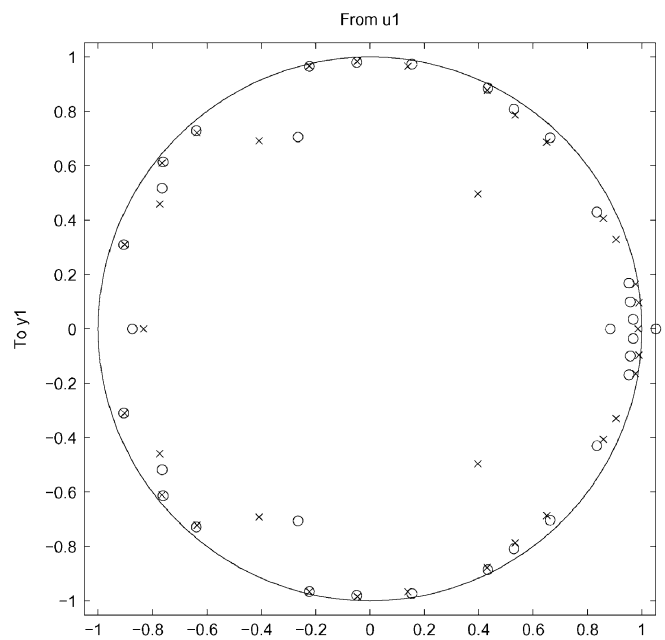

Fig. 15. Pole-zero plot for the computed linear model for case "B."

data. Excellent introductions to state-variable modeling and the system identification problem include [43] and [44]. Second, these models are ideally suited to solution via VHDL-AMS simulators [45], [46]. VHDL-AMS is an IEEE standard language for the coupled simulation of mixed discrete-time and continuous-time systems, and numerous simulators are available. The continuous-time systems are, in general, nonlinear differential-algebraic systems of equations and are integrated via adaptive algorithms [47], [48]. The VHDL-AMS approach has been previously used for modeling of RF circuits such as VCOs [49], [50], although without distributed electromagnetic effects.

For convenience, the MATLAB Signal Identification Toolbox was used to generate the behavioral models. This Toolbox contains algorithms for obtaining best fit linear state-variable models given input and output data, and it is straightforward to develop a high-level script that uses these built-in algorithms. The high-level script implements the following steps.

Step 1) Low-pass filter the response data.
Step 2) Decimate the response data to 200–500 samples.
Step 3) Estimate the delay between the response and excitation.
Step 4) Compute the best fit discrete model.
Step 5) Convert discrete mode to continuous-time model.

The first step eliminates unneeded and inaccurate high-frequency content from the response signal. The simulated electromagnetic response contains frequencies in the 0–500-GHz

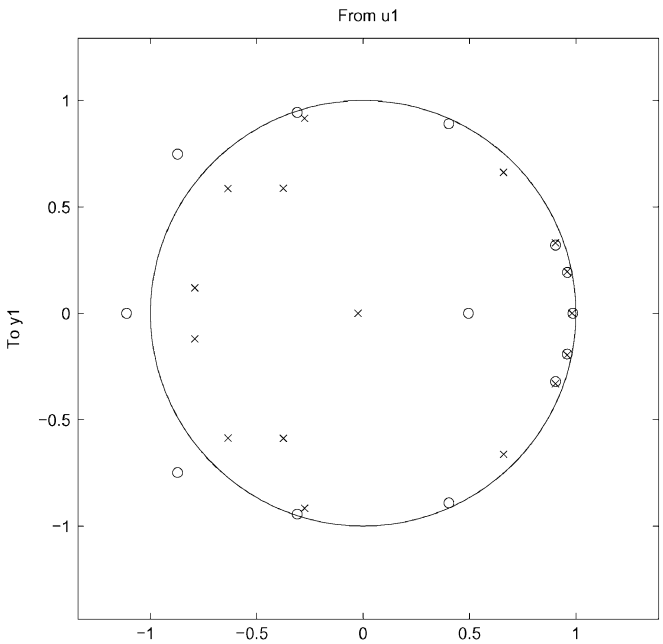

Fig. 16. Pole-zero plot for the computed linear model for case "F."

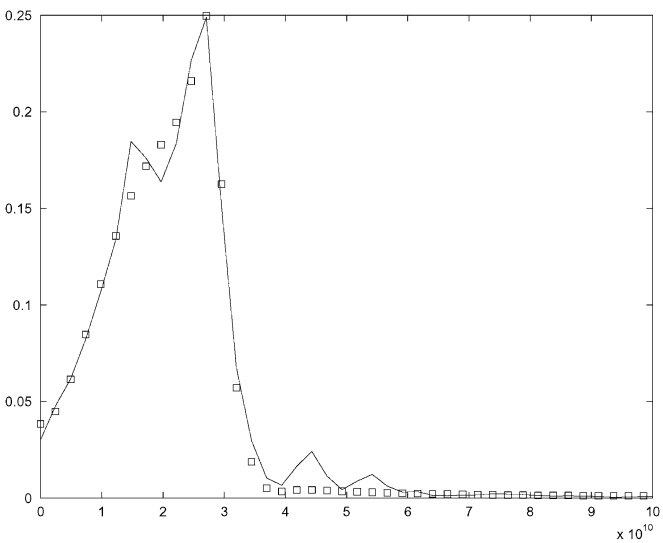

Fig. 17. Frequency response of the state-variable model compared to the actual signal for case "A." The model is designated by squares, the actual signal is the solid line.

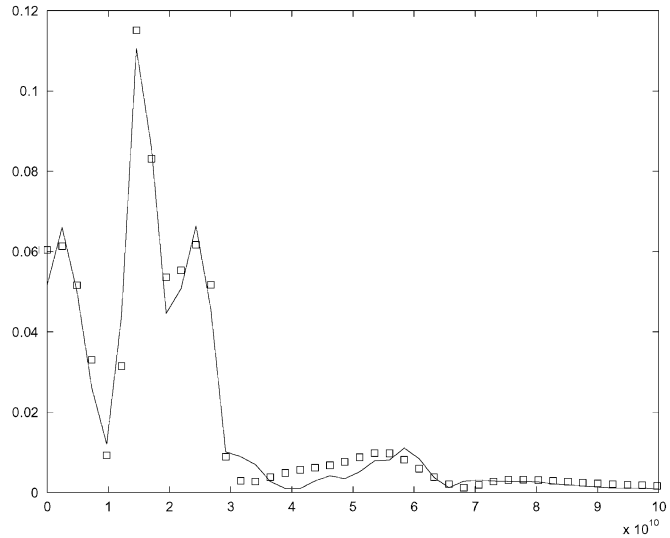

Fig. 18. Frequency response of the state-variable model compared to the actual signal for case "B." The model is designated by squares, the actual signal is the solid line.

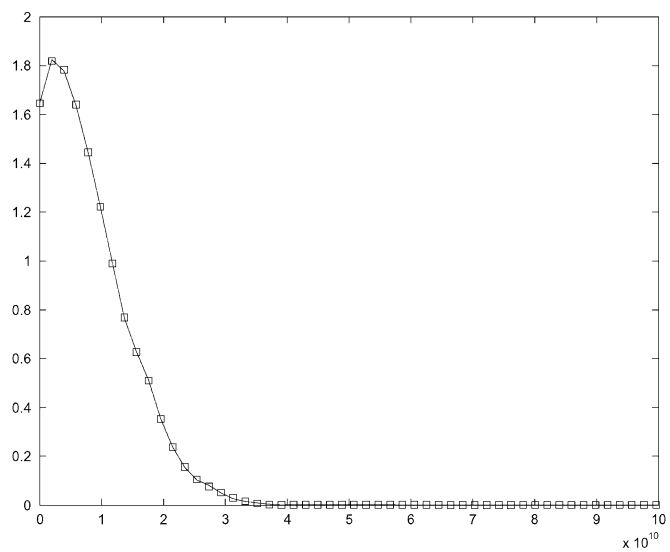

Fig. 19. Frequency response of the state-variable model compared to the actual signal for case "F." The model is designated by squares, the actual signal is the solid line.

range (determined by the simulation time step Δt), but only the 0–50-GHz range is of interest in this paper. The second step is not required, but does significantly speed up the computation of the state-variable model. The third step is critical, without a delay, a very high-order model will be required to model the response simply due to the delay. By explicitly taking into account the delay, a low-order model is obtainable. The fourth step is simply repeated for different model orders, and the best model is selected. In this paper, models were constrained to have an order less than 40. The final step converts the discrete-time model to a continuous-time model in the form given by (15).

A summary of the computed models is shown in Table I. The *delay* column is the estimated delay used to generate the best fit model, it may or may not correspond to the actual delay because the model itself has some intrinsic delay. The *max signal* column is the maximum absolute value of the response signal for a normalized (unit amplitude) excitation signal; it is a simple measure of the strength of the coupling between the input port and the output port. The *order* is the order of the best fit state-variable model, restricted to be less than 40. Finally, the *fit* column is a measure of the fit between the mode and actual data.

Comparison of the actual electromagnetic response with the model signal for cases "A," "B," and "F" are shown in Figs. 11–13. The pole-zero plots of the computed state-variable models are shown in Figs. 14–16. Note that no special effort was required here to obtain stable models, which is in contrast to frequency-domain pole-zero modeling. In the frequency domain, the pole-zero model that minimizes the mean-square error may not be stable, and additional constraints are required to obtain a stable model. For the time-domain state-variable

approach, if the response decays at a reasonable rate (low-Q) the best fit model will naturally be stable. The frequency response of the models are shown in Figs. 17–19. The models provide a good approximation of the true frequency response from 0 to 50 GHz. Obviously, higher order models would provide greater frequency resolution, but the intent here was to develop simple and efficient low-order models appropriate for VHDL-AMS simulation.

IV. Conclusion

In this paper, a procedure for the computer simulation and modeling of distributed electromagnetic coupling in ICs has been presented. The simulation has been performed using a full-wave time-domain finite-element method on 3-D unstructured computational meshes. This is a direct numerical simulation of Maxwell's equations, the accuracy of which is limited solely by computational resources, i.e., it is not a quasi-static or otherwise physically approximate approach. Therefore, the simulation includes parasitics, substrate currents, and electromagnetic radiation. This simulation approach is quite general and can be used for circuit layouts that include isolation wells, guard rings, and 3-D metallic structures. The specific finite-element method used here is second-order accurate in time and space, it correctly models the jump discontinuity of fields and currents across material boundaries, and it is energy and charge conserving. Due to the disparity in the size of the computational mesh elements, the Newmark-beta implicit time integration method is used to avoid the time-step restriction of explicit methods. The computer run time is dominated by the solution of the resulting linear system of equations. In this paper, a simple diagonally preconditioned conjugate gradient linear solver was used, and more advanced methods, such as multigrid or Schwartz methods, could significantly improve the situation, but were not studied here.

A state-variable behavioral modeling approach has been advocated for combining the results of the electromagnetic simulation with a VHDL-AMS circuit simulation. A procedure for generating the best fit state-variable model has been described, and results have been presented for a VCO test circuit. The models have been restricted to be low order for efficient circuit simulation. The resulting models are stable and valid from 0 to 50 GHz.

Acknowledgment

This study was performed under the auspices of the U.S. Department of Energy by the University of California, Lawrence Livermore National Laboratory, Livermore, CA.

References

[1] T. C. Edwards and M. B. Steer, *Foundations of Interconnect and Microstrip Design*. New York: McGraw-Hill, 1959.

[2] A. Niknejad and G. Meyer, *Design, Simulation, and Applications of Inductors and Transformers for Si RF ICs*. Norwell, MA: Kluwer, 2000.

[3] J. J. Zhou and D. J. Allstot, "Monolithic transformers and their application in a differential CMOS RF low-noise amplifier," *IEEE Trans. Solid-State Circuits*, vol. 33, pp. 2002–2027, Dec. 1998.

[4] R. Gupta, B. M. Ballweber, and D. J. Allstot, "Design and optimization of CMOS RF power amplifiers," *IEEE Trans. Solid-State Circuits*, vol. 36, pp. 166–175, Feb. 2001.

[5] K. Nabors and J. White, "FASTCAP: A multipole accelerated 3D capacitance extraction program," *IEEE Trans. Computer-Aid. Design*, vol. 10, pp. 1447–1459, Nov. 1991.

[6] M. Kamon, M. J. Ttsuk, and J. K. White, "FASTHENTRY: A multipole accelerated 3D inductance extraction program," *IEEE Trans. Microwave Theory*, vol. 42, pp. 1750–1758, Sept. 1994.

[7] J. R. Phillips and J. K. White, "A precorrected FFT method for electrostatic analysis of complicated 3D structures," *IEEE Trans. Computer-Aided Design*, vol. 16, pp. 1059–1072, Oct. 1997.

[8] S. Kapur and D. E. Long, "IES3: Efficient electrostatic and electromagnetic simulation," *IEEE Comput. Sci. Eng. Mag.*, vol. 5, pp. 60–67, Apr. 1998.

[9] A. M. Niknejad, R. Gharpurey, and R. G. Meyer, "Numerically stable Green function for modeling and analysis of substrate coupling in integrated circuits," *IEEE Trans. Computer-Aided Design*, vol. 17, pp. 305–315, Apr. 1998.

[10] A. M. Niknejad and R. G. Meyer, "Analysis, design, and optimization of spiral inductors and transformers for Si RF ICs," *IEEE Trans. Solid-State Circuits*, vol. 33, pp. 1470–1481, Oct. 1998.

[11] ——, "Analysis of eddy-current losses over conductive substrates with applications to monolithic inductors and transformers," *IEEE Trans. Solid-State Circuits*, vol. 49, pp. 166–176, Jan. 1998.

[12] D. K. Su, M. J. Loinaz, S. Masui, and B. A. Wooley, "Experimental results and modeling techniques for substrate noise in mixed-signal integrated circuits," *IEEE Trans. Solid-State Circuits*, vol. 28, pp. 420–430, Apr. 1993.

[13] N. K. Verghese, D. J. Allstot, and M. A. Wolf, "Verification techniques for substrate coupling and their application to mixed-signal IC design," *IEEE Trans. Solid-State Circuits*, vol. 31, pp. 354–365, May 1996.

[14] J. M. Casalta, X. Aragones, and A. Rubio, "Substrate coupling evaluation in BiCMOS technology," *IEEE Trans. Solid-State Circuits*, vol. 32, pp. 598–603, Apr. 1997.

[15] X. Aragones and A. Rubio, "Experimental comparison of substrate noise coupling using different wafer types," *IEEE Trans. Solid-State Circuits*, vol. 34, pp. 1405–1409, Oct. 1999.

[16] Y. Rolain, W. Van Moer, G. Vandersteen, and M. van Heijningen, "Measuring mixed signal substrate coupling," *IEEE Trans. Instrum. Meas.*, vol. 40, pp. 959–964, Aug. 2001.

[17] F. Martorell, D. Mateo, and X. Aragones, "Modeling and evaluation of substrate noise induced by interconnects," in *Design, Automation, and Test in Europe*, Mar. 2003, pp. 524–529.

[18] A. L. L. Pun, T. Yeung, J. Lau, F. J. R. Clement, and D. K. Su, "Substrate noise coupling through planar spiral inductor," *IEEE Trans. Solid-State Circuits*, vol. 33, pp. 877–884, June 1998.

[19] F. Herzel and B. Razavi, "Oscillator jitter due to supply and substrate noise," in *IEEE Custom Integrated Circuits Conf.*, 1998, pp. 489–3492.

[20] ——, "A study of oscillator jitter due to supply and substrate noise," *IEEE Trans. Circuits Systems II*, vol. 46, pp. 56–62, Jan. 1999.

[21] M. McCorquodale, M. K. Ding, and R. B. Brown, "Study and simulation of CMOS *LC* oscillator phase noise and jitter," in *Proc. Int. Circuits and Systems Symp.*, 2003, pp. 665–668.

[22] H.-T. Ahn and D. J. Allstot, "A 0.5–8.5 GHz fully differential CMOS distributed amplifier," *IEEE Trans. Solid-State Circuits*, vol. 37, pp. 985–993, Aug. 2002.

[23] C. Soens, C. Crunelle, P. Wambacq, G. Vandersteen, S. Donnay, Y. Rolain, M. Kuijk, and A. Barel, "Characterization of substrate noise impact on RF CMOS integrated circuits in lightly doped substrates," in *Instrumentation and Measurement Technology Conf.*, May 2003, pp. 1303–1308.

[24] R. Singh and S. Sali, "Modeling of electromagneticlly coupled substrate noise in FLASH A/S converters," *IEEE Trans. Elect. Comput.*, vol. 45, pp. 459–468, Feb. 2003.

[25] T. Yeung, A. Pun, Z. Chen, J. Lau, and F. J. Clement, "Noise coupling in heavily and lightly doped substrate from planar spiral inductor," in *IEEE Int. Circuits and Systems Symp.*, June 1997, pp. 1405–1408.

[26] W. Winkler and F. Herzel, "Active substrate noise suppression in mixed-signal circuits using on-chip driven guard rings," in *IEEE Custom Integrated Circuits Conf.*, 2000, pp. 357–360.

[27] A. Samavedam, K. Mayaram, and T. Fiez, "A scalable substrate noise coupling mode for mixed-signal IC's," *IEEE Trans. Solid-State Circuits*, vol. 35, pp. 895–904, June 2000.

[28] R. Singh, S. Sali, and W. L. Woo, "Efficient methods for modeling substrate coupling in mixed-signal integrated circuits," *Elect. Commun. Eng. J.*, pp. 237–248, Dec. 2001.

[29] N. K. Verghese and D. J. Allstot, "Substrate coupling in mixed-mode and RF integrated circuits," in *10th IEEE Int. ASIC Conf.*, 1997, pp. 297–303.

[30] ——, "Computer-aided design considerations for mixed-signal coupling in RF integrated circuits," *IEEE Trans. Solid-State Circuits*, vol. 33, pp. 314–323, Mar. 1998.

[31] N. Verghese, J. Schmerbeck, and D. Allstot, *Simulation Techniques and Solutions for Mixed-Signal Coupling in Integrated Circuits*. Norwell, MA: Kluwer, 1995.

[32] B. Stanisic, N. Verghese, R. Rutenbar, L. R. Carley, and D. J. Allstot, "Addressing substrate coupling in mixed-mode ICs: Simulation and power distribution synthesis," *IEEE Trans. Solid-State Circuits*, vol. 29, pp. 226–237, Mar. 1994.

[33] L. M. Silveira and N. Vargas, "Multilevel finite difference methods for the characterization of substrate coupling in deep sub-micron designs," *Integrated Circuits and Systems Symp.*, vol. XII, pp. 26–30, Sept. 1999.

[34] R. Garhpurey and R. G. Meyer, "Modeling and analysis of substrate coupling in integrated circuits," *IEEE Trans. Solid-State Circuits*, vol. 31, pp. 344–353, Mar. 1996.

[35] J. P. Costa, M. Chou, and L. M. Silveira, "Efficient techniques for accurate modeling and simulation of substrate coupling in mixed-signal ICs," *IEEE Trans. Computer-Aided Design*, vol. 18, pp. 597–607, May 1999.

[36] A. Bossavit, *Computational Electromagnetism: Variational Formulation, Complementarity, Edge Elements*. New York: Academic, 1998.

[37] M. Salazar-Palma, T. K. Sarkar, L. Garcia-Costillo, and T. Roy, *Iterative and Self Adaptive Finite Elements in Electromagnetic Modeling*. Norwood, MA: Artech House, 1998.

[38] J. Jin, *The Finite Element Method in Electromagnetics*, 2nd ed. New York: Wiley, 2002.

[39] D. White, "Numerical modeling of optical gradient traps using the vector finite element method," *J. Comput. Phys.*, vol. 159, pp. 13–37, 2000.

[40] G. Rodrigue and D. White, "A vector finite element time-domain method for solving Maxwell's equations on unstructured hexahedral grids," *SIAM J. Sci. Comput.*, vol. 23, no. 3, pp. 683–706, 2001.

[41] D. Jiao and J. Jin, "A general approach for the stability analysis of the time domain finite element method for electromagnetic simulations," *IEEE Trans. Antennas Propagat.*, vol. 50, pp. 1624–1632, Nov. 2002.

[42] D. White, "Numerical dispersion of a vector finite element method on skewed hexahedral grids," *Commun. Numer. Methods Eng.*, vol. 16, pp. 47–55, 2000.

[43] C.-T. Chen, *Linear System Theory and Design*. Oxford, U.K.: Oxford Univ. Press, 1998.

[44] L. Ljung, *System Identification: Theory for the User*. Upper Saddle River, NJ: Prentice-Hall, 1999.

[45] E. Christen and K. Bakalar, "VHDL-AMS: A hardware description language for analog and mixed-signal applications," in *IEEE Trans. Circuits Systems II*, vol. 46, Oct. 1999, pp. 1263–1271.

[46] P. Ashenden, G. Petersen, and D. Teegarden, *The System Designers Guide to VHDL-AMS*. San Mateo, CA: Morgan Kaufmann, 2002.

[47] A. Hindmarsh and L. R. Petzhold, "Algorithms and software for ordinary differential equations and differential-algebraic equations Part I: Euler methods and error estimation," *Comput. Phys.*, vol. 9, pp. 34–41, 1995.

[48] ——, "Algorithms and software for ordinary differential equations and differential-algebraic equations Part II: Higher-order methods and software packages," *Comput. Phys.*, vol. 9, pp. 148–155, 1995.

[49] A. Fakhfakh, N. Milet-Lewis, J. Thomas, and H. Levi, "Behavioral modeling of phase noise and jitter in voltage-controlled oscillators with VHDL-AMS," in *1st IEEE Circuits Systems for Communications Conf.*, June 2002, pp. 370–373.

[50] A. Fakhfakh, H. Levi, N. Milet-Lewis, and Y. Danto, "Behavioral modeling of analogue and mixed-signal integrated systems with VHDL-AMS for RF applications," in *15th Integrated Circuits and Systems Design Symp.*, Sept. 2002, pp. 308–313.

[51] J. C. Nédélec, "Mixed finite elements in r3," *Numer. Math.*, vol. 35, pp. 315–341, 1980.

[52] P. Monk, *Finite Element Methods for Maxwell's Equations*, ser. Numer. Math. Sci. Comput.. New York: Clarendon Press, 2003.

[53] D. Jiao, L. Mingyu, E. Michielssen, and J. Jin, "A fast time domain finite element boundary integral method for electromagnetic analysis," *IEEE Trans. Antennas Propagat.*, vol. 49, pp. 1453–1461, Oct. 2001.

[54] G. D. Smith, *Numerical Solution of Partial Differential Equations: Finite Difference Methods*, 3rd ed. Cambridge, U.K.: Oxford Univ. Press, 1986.

[55] S. D. Gedney and U. Navsariwala, "An unconditionally stable finite element time domain solution of the vector wave equation," *IEEE Microwave Guided Wave Lett.*, vol. 5, pp. 332–334, Oct. 1995.

Daniel A. White (M'88) received the B.S. and M.S. degrees in electrical and computer engineering and Ph.D. degree in applied science from the University of California at Davis, in 1985, 1986, and 1997, respectively.

From 1986 to 1993, he was a Senior Engineer with the Hughes Missile Systems Company (formerly Convair Division, General Dynamics), San Diego, CA. While with the Hughes Missile Systems Company, he was involved with inverse synthetic aperture radar imaging, radar target identification, and low-observable technology. In 1993, he joined the Lawrence Livermore National Laboratory, Livermore, CA, where he is currently Group Leader of the Computational Engineering Group of the Defense Sciences Engineering Division. His current research interests include higher order methods for computational electromagnetics, multiphysics simulations, and massively parallel computing.

Mark Stowell received the B.S. degree in physics and Master of Science degree in applied mathematics from the University of Massachusetts at Amherst, in 1992 and 1994, respectively.

Prior to joining the Lawrence Livermore National Laboratory (LLNL), Livermore, CA, he was a Computer System Administrator with the University of Massachusetts at Amherst. His interests include computational physics, numerical analysis, and parallel computing.